



Novel Bio-fabrication Modelling Approach from Marine Sources: Synthesis, Characterization and its Composite Formulations

Gunarajulu Renganathan¹, R. Dheivanai¹, Kalyani Durai¹, Suguna Lakshmi Madurai^{2*}

¹Division of Biomedical Engineering, Department of ECE, Anna University, Chennai 600025, India

²Polymer science and Technology Division, CSIR-Central Leather Research Institute, Chennai 600020, India

Received: 15 March 2021

Accepted: 6 April 2021

Published online: 23 February 2022

Keywords: hydroxyapatite, seashells, composite scaffold, bone tissue engineering

Hydroxyapatite, a bone mineral was extracted from different seashell species by hydrothermal method and investigated by SEM-EDX, FTIR, TGA, DSC, XRD, and EPR analysis. Amongst, the seashell *Dallarca subrostrata* was chosen for composite preparation by incorporating chitosan and silver nanoparticles which could be used as fillers and films for wound healing applications. Silver ions doped HA were examined using EPR for better biocompatibility. These findings further aim to create a patient-specific implant using 3D modelling. It paves the way for the potential applications as a pre-operative surgical planning procedure and a better point of health care. Further, the biominerals extracted would act as a source for the fabrication of designs and thereafter 3D modelling for investigation. It also rectifies tissue engineering challenges faced so far.

© (2022) Society for Biomaterials & Artificial Organs #20057922

Introduction

The emerging interest for reconstruction material for bone fixation has seen as a driving force in Tissue therapy and organ regeneration [1,2]. The current clinical remedy for bone imperfections incorporates grafting techniques [3,4], the structure of counterfeit bone scaffolds, surgical reconstruction, transplantation, drug delivery, artificial prostheses, and therapeutic devices which have been currently supplanted by means of additive technologies [5-8]. For example, 3D bio-fabrication platforms for patient-specific implants [9-11] so as to defeat the impediments like danger of infusions, hematoma, safe dismissal, contributor site grimness, and transmission of viral infections studied by earlier research works [12]. Current metallic inserts made of titanium, stainless steel, and cobalt-chromium amalgams for hip, knee and shoulder abandons get debased in due course of time [13,14]. Further, the latter technique would be increasingly critical in accomplishing the high porosity and load-bearing limit, corrosion resistive, non-carcinogenicity required for the bone scaffolds [15,16].

Bone comprises of both natural and inorganic constituents, of

which 70 wt% of the inorganic constituent represents the bone mineral named hydroxyapatite (HA). It is a notable mineral segment of human teeth and skeletal framework seen as a promising biomaterial, because of its unique attributes like osteoconductivity [17], biocompatibility [18], bioactive [19], bioresorbability [20], non-toxic, non-immunogenicity [21] which favour cell adherence, cell growth and mineralisation in the recovery process [22]. HA produced from the biogenic sources, for example, eggshells [23,24], bovine bone [25], fish bone [26], crab shells [27], corals [28], and nacreous [29] shows greater similarity with the human bone.

In the present investigation, HA acquired from the marine waste was subjected to the following investigations SEM-EDX, FT-IR, TGA, DSC, XRD, and EPR analysis. The results were used to confirm the morphological similarities and elemental compositions of HA from marine waste with that of the calcium derivate present in the natural bone.

Materials and Methods

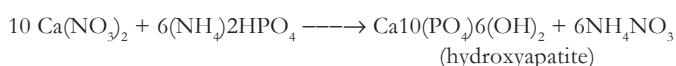
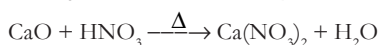
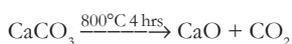
Diammonium hydrogen phosphate ((NH₄)₂HPO₄), Nitric acid (HNO₃), sodium hydroxide (NaOH), acetone, silver nitrate (AgNO₃), acetic acid (CH₃COOH), chitosan was obtained from Sigma-Aldrich (analytical grade).

* Corresponding author

msugunalakshnimadurai@gmail.com (Dr. Suguna Lakshmi Madurai, Polymer Science and Technology Division, CSIR-Central Leather Research Institute, Chennai 600020, India)

Synthesis of Hydroxyapatite (HA)

The resource used for the synthesis of hydroxyapatite (HA) by the hydrothermal method is a biowaste (seashells) from marine environment. According to the literature [30-32], the protocol includes two phases CaO production and the conversion of CaO to HA which are explained in detail below. Seashells collected were washed, dried in a hot air oven at 80°C for 3h, then granulated by mortar and pestle followed by calcination in a muffle furnace at 800°C for 4h prompts the production of CaO (white in nature). The blend was completely broken down in 25% of conc. HNO₃ and deionized water to form calcium nitrate (Ca(NO₃)₂). To this mixture, 0.6M of (NH₄)₂HPO₄ was added drop by drop to acquire Ca/P proportion as 1.67. 1M of NaOH was added gradually to keep up the pH of the blend as 9.0. The resultant was subjected to aging process for about 48h, after which the agglomerated precipitate was isolated and dried in hot air oven at 80°C for 2h and then repeatedly calcinated at 800°C for 3h to acquire HA, as a product.



Composite formulation

Preparation of silver doped hydroxyapatite (Ag-HA)

150 ml of AgNO₃ nanoparticles were dissolved in 60 ml of distilled water and stirred continuously for 4h. Further, 1.5g of HA were added to the mixture, stirred magnetically for about 2h. The resultant dried sol was kept in oven at 80°C for 2h which inevitably brings doping of silver to HA nanoparticles, as a bio-composite [33].

Preparation of Hydroxyapatite-Chitosan (HA-CS)

In the preparation of HA-CS composite as film and porous scaffold, 1.2g of HA were dissolved in 60% (2 vol %) of acetic acid followed by the addition of distilled water, the whole content was stirred for 2h. Likewise, 1.8g of chitosan were dissolved in 40ml of deionised water and mixed completely. Both the blends were combined and kept in a constant magnetic stirrer for around 90 min. The subsequent sol was added to the petri dish for the film development and further poured in a 12-well culture plate (2ml per well). Then, the composite HA-CS films were formed by drying at 37°C for 24h and the porous HA-CS scaffolds were shaped by freeze-drying [34].

Characterization

The morphology of HA samples was observed using Scanning electron microscopy (SEM; FEI Quanta) simultaneously coupled with Energy Dispersive X-Ray (EDX; FEI Quanta) spectroscopy for elemental analysis. The crystalline nature and phase composition of HA were determined through X-ray powder diffraction (XRD; Bruker) with Cu K α radiation, 2 θ = 10-80° operating at 30 kV and 15 mA by one step increment with a speed of 0.0005/deg. The HA associated functional groups were characterized using FT-IR (GX-Perkin Elmer) in the Attenuated Total Reflection (ATR) mode and the transmittance was found to be in the regions of 4000-400cm⁻¹. The thermal stability and weight loss with respect to temperature was found by thermo gravimetric analysis and differential scanning calorimetry analysis (TGA, DSC; LABSYS EVO) at a heating rate of 10°C/min in a nitrogen atmosphere. The free radicals were trapped using the X-band electron paramagnetic resonance spin technique (EPR; JOEL) with the spectrum as the energy absorbed when applying energy to an unpaired electron.

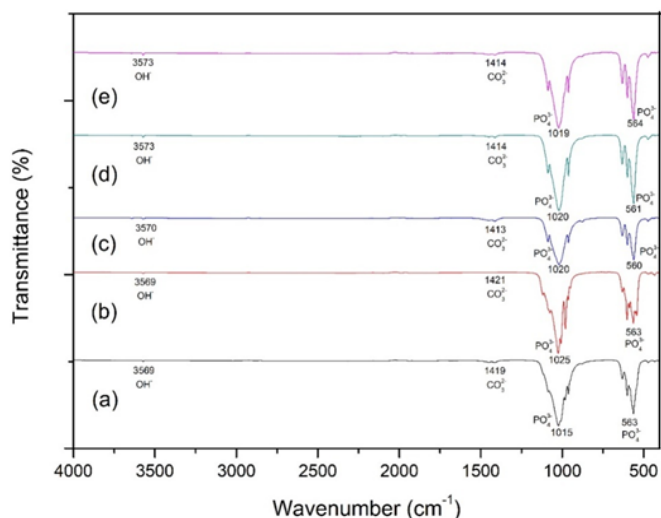


Figure 1: FTIR spectra of seashells (a) *Anadara pumila*, (b) *Agriopoma texasianum*, (c) *Dallarca subrostatata* (Ark shell), (d) *Glycymeris pectunculus* (spotted clam seashell), (e) *Astartidae castanea* (Polished Fossil astarac clam)

Results

Fourier Transform Infrared Spectroscopy (FTIR) analysis

FTIR was used to find the functional groups and their associated phase transition of the shells (a-e) at different wavelength. All the samples (a-e) were collected, calcinated at 800°C and the absorption spectra were recorded. The spectrum representation reveals its peak positions and intensities. Absorption data depicted were well associated with the XRD results [35]. The four essential vibrational modes (ν_1 , ν_2 , ν_3 and ν_4) for phosphate ions were found in the apatite phase, all of which are high IR active. Figure 1 depicts the IR spectra of the synthesized HA.

The broad and strong intensified IR band around the region of 1000–1100 cm⁻¹ is a major representation for the formation of HA. At 800°C, the high intense sharp peak observed at 3569- 3573cm⁻¹ is due to the absorption of water. This indicates the conversion of CaCO₃ to the CaO phase. This is supported by another evidence that reveals no bands formation were observed around 1410-1425 cm⁻¹ which indicates the absence of carbonate groups. The peaks found at 1015-1025 cm⁻¹ was due to the asymmetric stretching vibration (ν_3) mode of the major phosphate group and also the peaks found at 560 cm⁻¹ and 564 cm⁻¹ were also caused by the doubly degenerate bending mode (ν_4) of the P–O bond [36].

The peaks found around the regions of 600-620 cm⁻¹ indicate the HPO₄²⁻ ion vibrations show the weak existence of TCP due to the pH maintenance at 9.0. Thus, all the FTIR peaks found in the spectrum analysis strongly depicts the formation of HA. The present study clearly states the decrease in calcite intensities, decomposition of CaCO₃, formation of CaO at 800 - 900°C, and also the purity of HA extraction by the hydrothermal method [37].

Scanning electron microscopy (SEM) analysis

The morphology and fidelity in the shape of hydroxyapatite nanoparticles were characterized using SEM. The microstructural images reveal the distinct aggregation of nanoparticles and interconnected porous structures. The nanocrystalline molecules formed, which are bulky in nature, are agglomerated and of irregular pattern clearly indicates the pores in between them. The pore

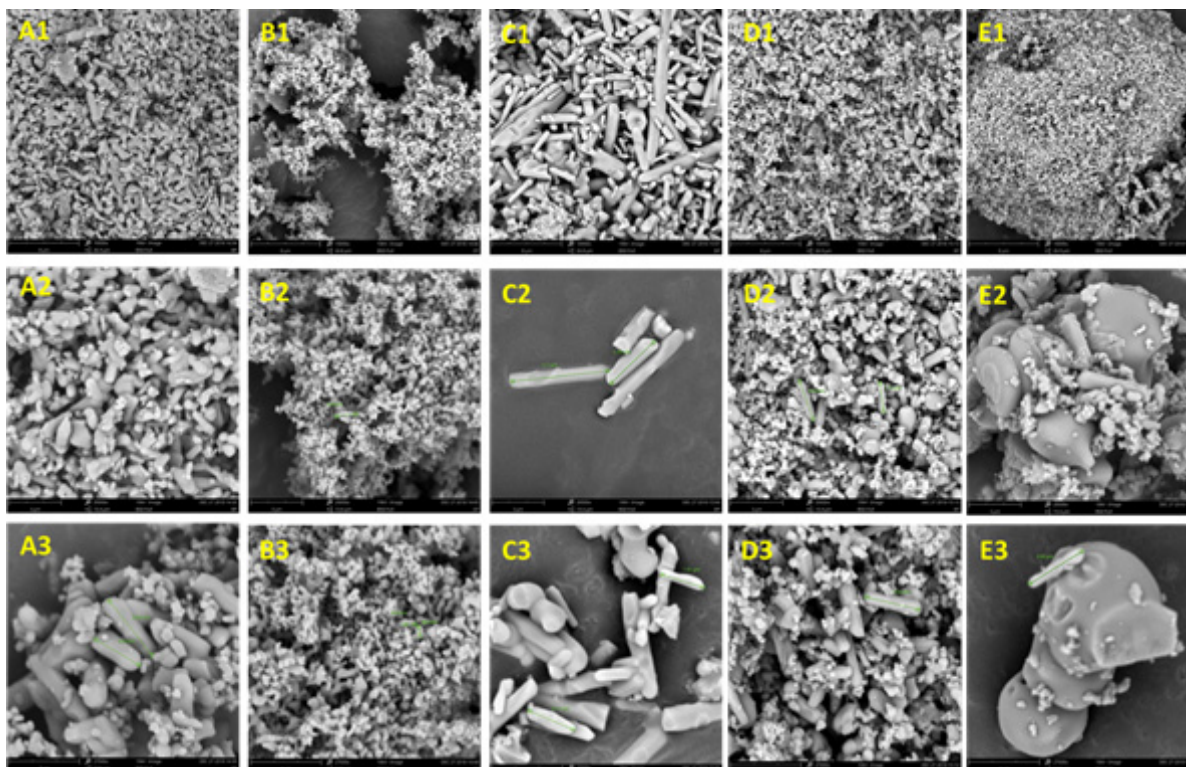


Figure 2: SEM images of seashells (A) *Anadara pumila*, (B) *Agriopoma texasianum*, (C) *Dallarca subrostrata* (Ark shell), (D) *Clycymeris pectunculus* (spotted clam seashell), (E) *Astartidae castanea* (Polished Fossil astartae clam) with different resolutions. (1) indicates magnification at 10000 \times , (2) indicates magnification at 20000 \times , (3) indicates magnification at 27000 \times

formation aids in cellular regeneration and promotes ingrowth of cells on the biological implants in the body [38]. Innumerable agglomerated collection of spherical and rod-like structures of smaller and larger particles was observed in figure 2 (a),(b) and (d) at different magnifications. In figure 2 (c), predominantly rod like structures were noticed, the individual crystals were well-defined at higher magnifications, whereas in figure 2E, unlike other SEM images the rhombus structure is also observed.

The rod-shaped HA nanoparticles observed from the SEM images were well-dispersed and their average size of the nanohydroxyapatite was found to be $\sim 2\text{-}3\ \mu\text{m}$ in A, $400\text{-}800\ \text{nm}$ B, $\sim 1\text{-}6\ \mu\text{m}$ in C, $\sim 1\text{-}2\ \mu\text{m}$ in D and $\sim 1\text{-}3\ \mu\text{m}$ in E respectively [39].

Energy dispersive X-ray (EDX) spectroscopy analysis

In order to identify the surface elemental composition, present in the seashell derived hydroxyapatite (HA) produced by the hydrothermal method elemental analysis using the EDX method was employed. This analysis gives the amount of calcium and phosphorous present in the sample and also the weight and atomic percentage of the element. The Ca/P ratio of ideal HA is 1.67 [40]. The element content of the calcinated HA was summarized in supplementary.

X-ray diffraction (XRD) spectroscopy analysis

The diffraction pattern obtained from the synthesized nHA samples is in fine agreement with those standard HA crystallites, (JCPDS card No. 09-432) respectively [41]. Furthermore, there was no incorporation of secondary trace elements in the XRD pattern. This confirms the purity of the nHA crystalline phase produced in

the test samples (a-e). This observation also indicates that pH is an essential criterion in determining the purity of phase apatite, which is an ideal factor in the hydrothermal method. Broad peaks reveal the nature of nanoparticles which is a key influencing factor in the particle size. The misalignment in the diffraction peaks may be due

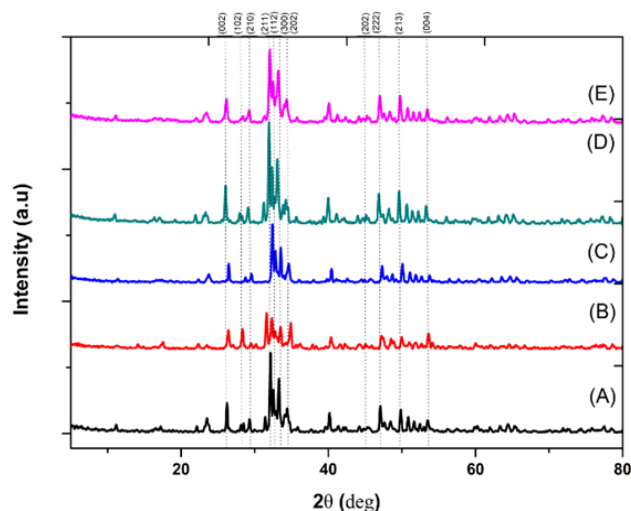


Figure 3: XRD patterns of seashells (a) *Anadara pumila*, (b) *Agriopoma texasianum*, (c) *Dallarca subrostrata* (Ark shell), (d) *Clycymeris pectunculus* (spotted clam seashell), (e) *Astartidae castanea* (Polished Fossil astartae clam)

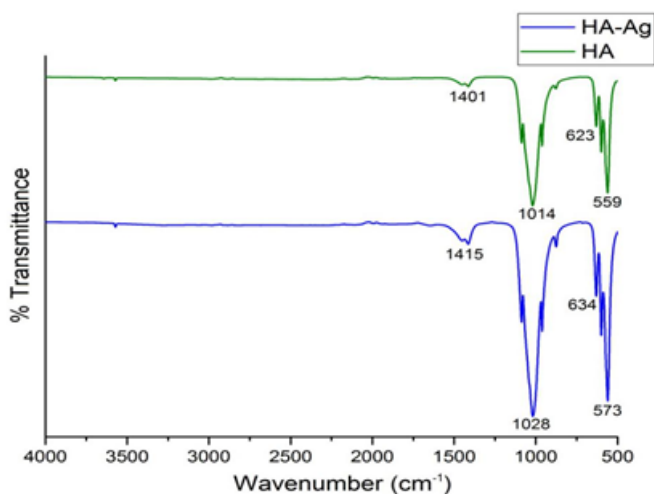


Figure 4: FTIR spectra of Ag-doped HA

to lattice structural changes, residual stress absorption, and defect concentration. The average crystallite size of nHA samples was calculated using Debye–Scherrer’s equation is attached in supplementary.

$$D_{hkl} = \kappa\lambda / \beta \cos\theta \text{ (nm)}$$

where $K = 0.94$ is a constant, λ is the wavelength of monochromatic radiation ($\lambda = 1.5405 \text{ \AA}$), and β is defined as the diffraction peak for full width at half maximum. The crystallite size D_{hkl} and the degree of crystallinity (X_c) was calculated based on the previous studies as follows,

$$X_c \text{ (\%)} = (\text{area of crystalline peaks} / \text{area of all peaks}) \times 100$$

Their main characteristics are summarized in the supplementary. From the data obtained, there is a strong decrease in the crystallite size of the synthesized HA is clearly indicated. The average size of the apatite crystal was calculated using an isolated diffraction peak ($2\theta = 26^\circ$) corresponding to the (002) plane. From the XRD peaks, HA nanoparticles synthesized at pH 9, the fraction of crystallinity was $\sim 0.99\%$ for crystallites 20-30 nm in size. Normally, nHA particles with low crystallinity ($\sim < 20 \text{ nm}$) were desirable for biomedical applications exhibits *in vivo* resorbable material property [35].

Thermo-gravimetric analysis (TGA)

Thermo gravimetric analysis (TGA) and differential thermal analysis (DTA) were done, starting from room temperature to 900°C at the heating rate of $10^\circ\text{C}/\text{min}$. TGA curves demonstrate the three stages of weight loss in the samples in the temperature ranging from 49°C to 188°C , 232°C to 580°C , 600°C to 1100°C . Stage 1 represents the evaporation of absorbed water; stage 2 represents crystallization of HA and the presence of solvent molecules. The stage 3 represents the ammonia removal from the gel, breakdown of CO_3^{2-} and HPO_4^{2-} ions, and the degradation of intermediate species during the synthesis process respectively. The total weight loss obtained was low and hence it is proved that the synthesized HA can withstand high temperatures [38,42].

Differential scanning calorimetry (DSC) analysis

The DSC analysis is a thermo analytical technique used for estimating the amount of energy absorbed or released by a sample when it is subject to heating or cooling.

This analysis provides the quantitative and qualitative data on endothermic (heat absorption) and exothermic (heat evolution) processes. The peak at 105.31°C corresponds to the endothermic reaction and 315.86°C corresponds to the exothermic reaction. A peak at 360°C - 420°C is due to the crystallization of hydroxyapatite. No major loss was found up to 500°C which shows the thermal stability of the HA powder with a stable curve within the temperature range. These results are favourable to attain monophasic biomaterial [38,43].

Characterization of hydroxyapatite composite (Ag-doped HA, HA-CS)

Among the five marine sources, sample-c *Dallarca subrostrata* (*Ark shell*), found to be more suitable for bone engineering applications. Hence, the composite formulation has been focussed and restricted with sample C and considered as a test sample for further doping and additional investigations.

FTIR of Ag-doped HA composite

Figure 4 shows the FTIR spectrum corresponding to HA and Ag-HA nanocomposite respectively. The band observed at 559 cm^{-1} was due to the bending vibration of the phosphate functional group (PO_4^{3-}) of HA. The peak at 623 cm^{-1} represents the stretching and bending bands for OH-group respectively and 1014 cm^{-1} can be considered as the breathing modes of the P-O stretching vibrations. The broad peaks at 3458 cm^{-1} were associated with the presence of OH group corresponds to H–O–H bands of water

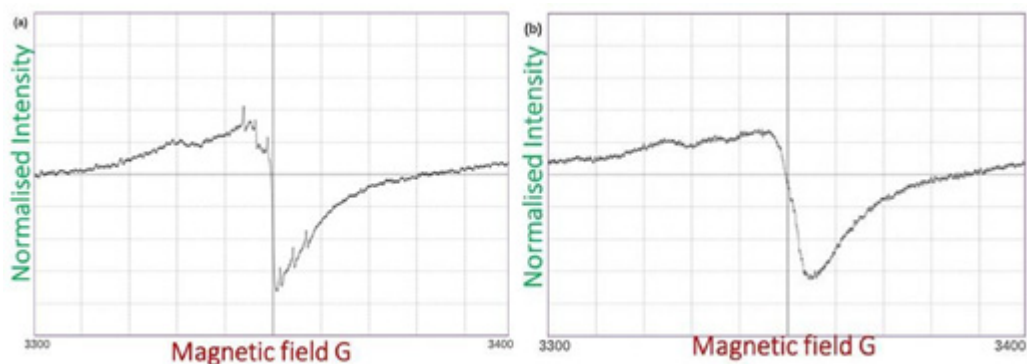


Figure 5: (a) EPR analysis of HA (b) EPR analysis of Ag doped HA

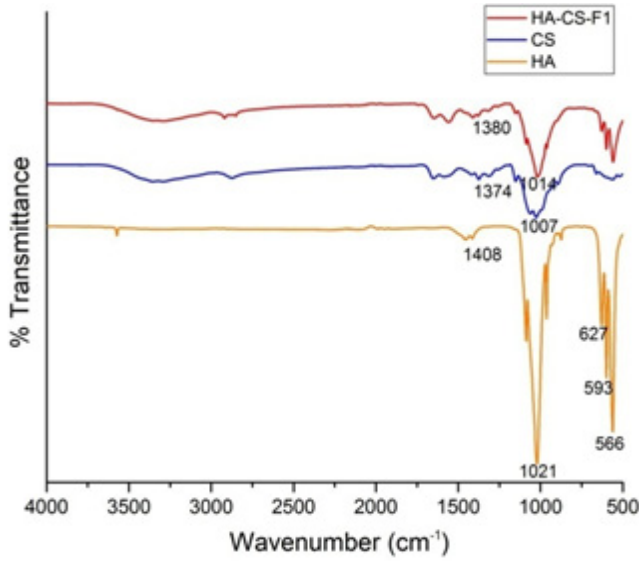


Figure 6: FTIR spectra of HA-CS

lattice possibly might be due to the absorbed water.

Ag-doped HAP shows the prevalence of phosphate bending peaks around the wave number 563 cm⁻¹ depicts the presence of HAP.

The existence of phosphate groups in close to apatitic proximity was revealed by the presence of major bands at 634 cm⁻¹ and 1028 cm⁻¹ in the FTIR spectrum of Ag⁺ doped HAP.

The shift in the peak from 3458cm⁻¹ to the higher range of 3625 cm⁻¹ in Ag-doped HAP attributes to the decrease in the water content which is mainly due to the substitution of Ag NP into Ca²⁺ apatite lattice. This suggests that Ag-HAP interaction has created structural changes in the nanocomposite.[33]

The FTIR spectra of nanocomposite show the presence of CO₃²⁻ around the wave numbers 1415 cm⁻¹ explains the stretching band of carbonate groups which indicates that not all the calcites were decomposed.

Electron paramagnetic resonance (EPR) analysis of Ag-doped HA

The experimental investigations of free oxygen radicals rely on EPR measurements of pure HAP as well as Ag-doped HAP at normal room temperature and the absorption spectra were shown in figure 5(a) and (b), clearly depicts the impact of unpaired electron of the metal complexes in the structural elucidation. The fine sharp peak in figure 5 (a) shows the hyperfine splitting of the spectrum which reveals the high intensity of electronic interaction in the HAP [44]. The anisotropic broad signal at g = 2.003 in Ag doped HAP in figure 5 (b) confirms the formation of free radicals which implies the inclusion of silver in the lattice of HAP.

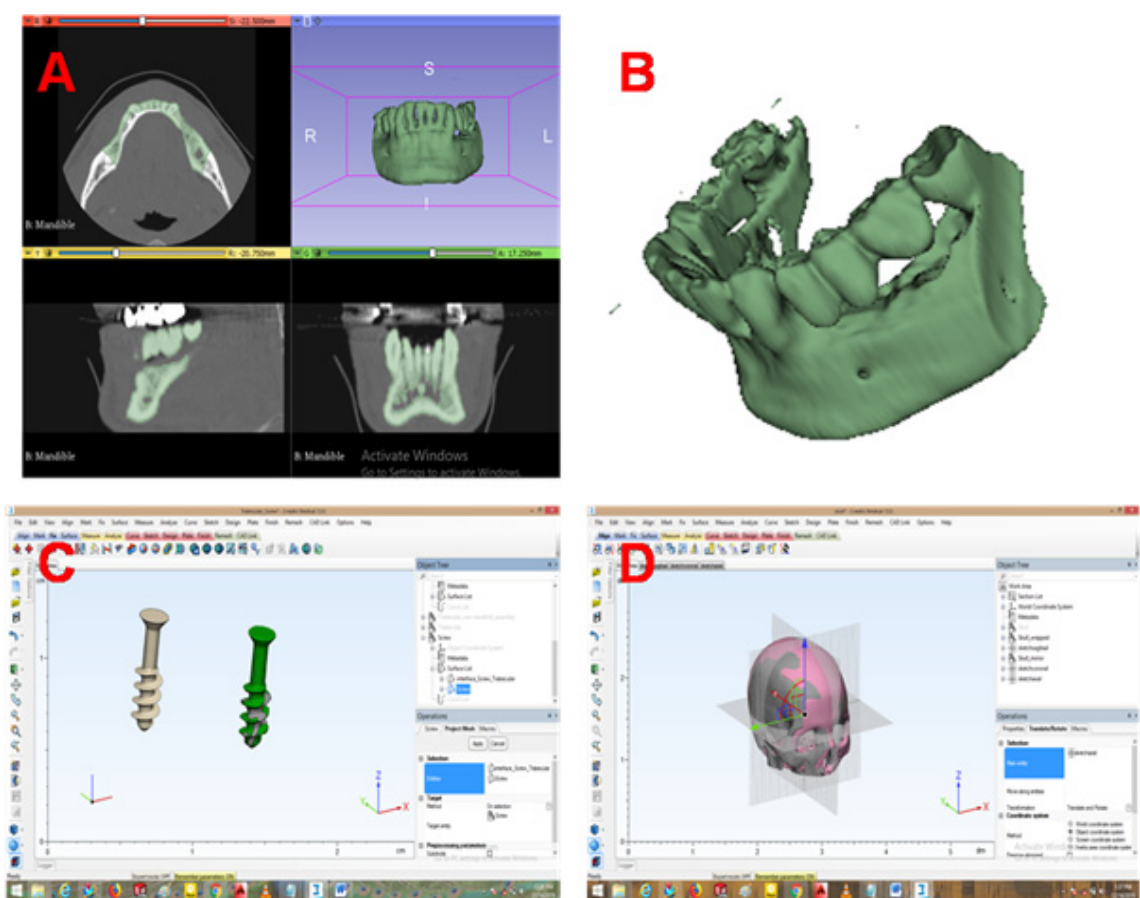


Figure 7: Novel clinical approach for Bio-fabrication [A –B] Mandible Reconstruction, [C] – Femur screw and [D] – Craniofacial implant design

FTIR of HA-CS composite

From IR spectroscopy of HA-CS composites, all the major absorbance bands of the spectra inferred were correspond to HA, their incremental width significantly shows the increase in chitosan content which was shown in figure 6. The bands at 1000-1100 cm^{-1} and 500-600 cm^{-1} correspond to different modes of the PO_4 group in HA. Broaden band near 1000 cm^{-1} shows the presence of polymer and its interaction with the phosphate groups. The bands at 1400-1500 cm^{-1} and about 875 cm^{-1} is due to the carbonate ions in apatite. The bands at 1550-1700 cm^{-1} is attributable to the mode superposition of the HA -OH group and the chitosan amide I and amide II groups. The bands at 3600-3700 cm^{-1} and 2800-2950 cm^{-1} is assigned to the hydroxyl groups present in chitosan. The hydroxyapatite phosphate stretching (vibration) bands at 1000-1100 cm^{-1} and the phosphate bending bands at 500-600 cm^{-1} . The strongest characteristic CO_3 bands are also visible, at 1420-1485 cm^{-1} . The FTIR investigation aids in confirming the presence of chitosan and its assimilation in the HA complex [45].

3D modelling

3D Modelling consolidates computer-aided design, which assists with pre-preparing (fitting) abilities. To do as such, it takes a shot at triangulated (STL) records, and all things considered are very reasonable for freestyle 3D information, similar to the anatomical information originating from the sections of radiological images. Import the anatomical information in the 3D modelling platform to study the models. The accompanying advances were pursued for the displaying procedure. For constructing a complex anatomical structure, arranging and reframing of bone could be done utilizing a 3D programming bundle. The creation can be made by utilizing the composite orchestrated for better biocompatibility with the 3D bioprinter. The steps for 3D Modelling were clearly explained below as follows. The clinical approach for fabricated was depicted in figure 7.

3D modelling implementation protocol

1. Collection of scanned datasets of injured patient data in (.dcm) DICOM format.
2. Stack of images collected were visualized in 3D DICOM viewer-based software such as Materialize MIMICS®, 3D Slicer®, etc., via 3 cardinal planes. (Transverse, Coronal and sagittal plane)
3. Selecting the fractured bone in the 3 planes by moving the slices in the appropriate planes and then performing segmentation using image processing toolkits
4. Performing segmentation based on histogram would yield better 3D volumetric reconstruction of the fractured bone.
5. Surgical planning involves the construction of fracture bone with suitable support structures for surgery which also be analysed using analysis toolkits such as FEA, COMSOL® based software for mechanical properties.
6. The mechanical properties of biomaterials were cross-checked with the properties of the bone which could be useful for planning in fabrication and also for studying the design complexities from the patient point of view
7. Implant design should be within the standard regulation protocol and also be supportive to the patient by reducing complexities and make them regain their normal mobility.

Discussion

Bone consists of both natural and inorganic components among which HA, is the major inorganic constituent. Choosing marine shells which has enormous calcium carbonate, act as a potential

source of HAP is a compelling way for minimizing the biowaste to an extent that could reduce the ecological contamination. From the above strategy, hydroxyapatite which is absolutely inorganic in nature when blended with metal ions might increase bioactivity, a crucial criterion for biomedical applications.

The morphological examination of HA powder using Electron Microscopy disclosed the structure of hydroxyapatite. From lower to the higher magnification of SEM images, homogeneously dispersed and uniform pattern of nanorods were observed with elongated shapes and prominent structure, suitable for drug delivery applications by agglomeration which preserves the nature of nanostructures. This indicates that the high temperature was helpful to improve the crystallinity of HA synthesized based on the hydrothermal approach. Moreover, nanorods obtained were extremely effective in building the framework suitable for cellular growth which might be suitable for wound healing applications. The EDX investigation of orchestrated HA shows that Ca/P proportion was 1.67 which correlated well with a theoretical value, implies calcium and phosphorous are the basic constituents of HAP and their contributions were similar to that of the natural existing bone.

The Fourier Transform Infrared Spectroscopy (FT-IR) results confirm the presence of functional groups in the composites, reveals that the sharp peaks acquired at high temperature are due to the rapid movement of vibrating molecules. The CO_3^{2-} and mass of other contaminants decreases after the calcination process. The proximity of phosphate groups shows the establishment of HA during the precipitation reaction, which was also supported by EDX investigation.

The thermal stability and the weight loss of HA were assessed by TGA up to 1000°C revealed that there was a base weight reduction in the powder, the results obtained were similar to that of hydroxyapatite extracted from the natural bone, which was a rich source for calcium has the ability to withstand thermal heat even at elevated temperatures. TGA investigation shows that there was no massive weight reduction up to 200°C and the reduction was observed as 1.36%, 0.65%, 1.79%, 0.05%, and 2.01% individually for the various marine shells. The freedom of synthetically reinforced water and disintegration of carbonate were seen between the ranges of 200°C to 600°C. It affirms the crystallization of HA powder with stable bend was seen within the temperature range.

In DSC bend, the initial rise and consistent fall show the existence of changes throughout the process of thermal treatment. The sharp peaks around 400°C show the crystallization of HA. Thus, the synchronizing results of TGA and DSC investigations aids in understanding the thermal properties of the incorporated HA which is a crucial and appropriate factor for biomedical applications. The XRD diffractograms of the compound show the nanocrystalline structure of HA, the maximum peak occurs at 800°C for 4 hrs. The crystallization of the powder was determined utilizing the force at (002) plane. The (h k l) records with gem planes affirm its purity, hexagonal structure, and phase arrangement of HA. An ESR reveals that the broad spectrum of Ag-doped HAP suggests the formation of reactive species due to the inclusion of silver in the nanocomposite while the high intensity of hyperfine structure observed in HAP depicts a depletion of free radicals. This might also impart scavenging and antimicrobial property to Ag-doped hydroxyapatite, a crucial requirement for the attainment of bone implants.

Conjuring HA content along with minerals could be appreciated towards the Patient-Explicit implant structuring which could be an additional favourable circumstance for the novel bone

reconstruction. The advantage over this concept will be very much useful to the clinician to perform pre-operative surgery planning with respect to the cellular environment of the patient. In addition, the level of complexity could also be reduced for better-targeted size of wound or injury that need to be fixed. Bio-manufacturing based fabrication methods would increase the suitable delivery of scaffold as per the needs would be clearly visualized with this state-of-the-art technology. Patient-specific customized fabrication would create the potential value of tissue engineering with a micro-architectural matrix for tissue growth factor and spatial control over the 3D bioprinting technologies.

Conclusion

The novelty in the current research encompasses the biogenic source sea shell changed into a crucial hydroxyapatite for biomedical applications. Biowaste gives an unpleasant odour, microbial augmentation and emanates CO₂ to a lesser degree as they are biodegradable and lead to ecological contamination. To reduce the contamination in an eco-friendly approach, hydroxyapatite has been sourced from the shells by the hydrothermal method. The FT-IR spectra reveal the transition of phase from aragonite to calcite, the close proximity of CO₃²⁻, PO₄³⁻ retention groups show the arrangement of HA, the blend doesn't contain any appreciable crystalline contamination. SEM findings clearly observe the grain and rod-like structures. TGA and DSC confirm the accuracy of HA powder. The current investigation prescribes an eco-friendly approach with minimal effort for the extraction of hydroxyapatite (HA).

In the current strategy, the biowaste seashell can be successfully recycled, the best method for bioremediation as well as an effective way of constructing a litter-free environment. 3D Modelling, a clinical approach that paves way for betterment in health care and an add on value to patient-specific customization, rapid recovery, pre-operative surgical procedures. This ideology gives a clear insight into tissue engineering with a microarchitectural level of spatial control and engineering the medical problems in a contemporary manner.

Future Work

At present metals like steel, titanium and cobalt-chromium based combinations are widely used as an embedded material, in constructing hip, knee, shoulder, and elbow implant for load-bearing applications. In a stipulated time, intense research in bioactive materials that supersedes metallic inserts has been carried out. As a construct, it has progressively hoped to incorporate composite materials with extended bioactivity which favours cell growth. In future, to enhance osteogenesis and chondrogenesis on nanocomposite, it's crucial to achieving more intense screening on mechanical and biochemical properties that are mandatory for the cells to enhance vasculogenesis. This may be achieved by improvising the strategies in fabrication techniques and computational manifestation. Therefore, the up gradation in the technological aspect, is more useful for the betterment of human health in an affordable manner.

References

1. Zeeshan Sheikh et al., Biodegradable Materials for Bone Repair and Tissue Engineering Applications, *Materials*, 8(9), 5744–5794 (2015).
2. Kevin Dzobo et al., Advances in Regenerative Medicine and Tissue Engineering: Innovation and Transformation of Medicine, *Stem Cells International*, 2018, article ID 2495848 (2018).
3. Wenhao Wang et al., Bone grafts and biomaterials substitutes for bone defect repair: A review, *Bioactive materials*, 2(4), 224-247 (2017).
4. V. Campana et al., Bone substitutes in orthopaedic surgery: from basic

science to clinical practice, *Journal of Materials Science: Materials in Medicine*, 25(10), 2445–2461 (2014).

5. A. Aimar, A. Palermo, B. Innocenti, The Role of 3D Printing in Medical Applications: A State of the Art, *Journal of Healthcare Engineering*, 2019, article ID 5340616 (2019).
6. T. Wu et al., Bionic design, materials and performance of bone tissue scaffolds, *Materials*, 10(10), 1187–1187 (2017).
7. J. Henkel et al., Bone regeneration based on tissue engineering conceptions - a 21st century perspective, *Bone research*, 1, 216-248 (2013).
8. A.A. Zadpoor. J. Malda, Additive manufacturing of biomaterials, tissues, and organs, 45, 1-11, (2017).
9. K. Tappa, U. Jammalamadaka, Novel Biomaterials Used in Medical 3D Printing Techniques, *Journal of Functional Biomaterials*, 9(1), 17–17 (2018).
10. D. Martinez-Marquez et al., Application of quality by design for 3D printed bone prostheses and scaffolds, *PloS one*, e0195291 (2018).
11. G. Turnbull et al., 3D bioactive composite scaffolds for bone tissue engineering, *Bioactive materials*, 3(3), 278-314 (2018).
12. J.A. Fishman, Infection in Organ Transplantation, *American Journal of Transplantation*, 17(4), 856–879 (2017).
13. V. Sansone, D. Pagani, M. Melato, The effects on bone cells of metal ions released from orthopaedic implants. A review, *Clinical Cases in Mineral and Bone Metabolism*, 10(1), 34-40 (2013).
14. Kang, Cheng-Wei, Feng-Zhou Fang, State of the art of bioimplants manufacturing: part I, *Advances in Manufacturing*, 6, 20-40 (2018).
15. Meenakshi Mour et al., Advances in Porous Biomaterials for Dental and Orthopaedic Applications, *Materials*, 3(5), 2947–2974 (2010).
16. Chengde Gao et al., Bone biomaterials and interactions with stem cells, *Bone research*, 5, 1-33 (2017).
17. Joseph R. Woodard et al., The mechanical properties and osteoconductivity of hydroxyapatite bone scaffolds with multi-scale porosity, *Biomaterials*, 28(1), 45–54 (2007).
18. H Wang et al., Biocompatibility and osteogenesis of biomimetic nano-hydroxyapatite/polyamide composite scaffolds for bone tissue engineering, *Biomaterials*, 28(22), 3338–3386 (2007).
19. G. Suresh Kumar et al., Synthesis and characterization of bioactive hydroxyapatite–calcite nanocomposite for biomedical applications, *Journal of Colloid and Interface Science*, 349(1), 56–62 (2010).
20. Konrad Szustakiewicz et al., The influence of hydroxyapatite content on properties of poly(L-lactide)/hydroxyapatite porous scaffolds obtained using thermal induced phase separation technique, *European Polymer Journal*, 113, 313–320 (2019).
21. Maddela Swetha et al., Biocomposites containing natural polymers and hydroxyapatite for bone tissue engineering, *International journal of biological macromolecules*, 47(1), 1-4 (2010).
22. G Sui et al., Poly-L-lactic acid/hydroxyapatite hybrid membrane for bone tissue regeneration, *Journal of Biomed Materials Research A*, 82(2), 445–54 (2007).
23. Himanshu Khandelwal, Satya Prakash, Synthesis and Characterization of Hydroxyapatite Powder by Eggshell, *Journal of Minerals and Materials Characterization and Engineering*, 4(2), 119–126 (2016).
24. Gréta Gergely et al., Preparation and characterization of hydroxyapatite from eggshell, *Ceramics International*, 36(2), 803–806 (2010).
25. R. Nirmala et al., Synthesis and characterization of bovine femur bone hydroxyapatite containing silver nanoparticles for the biomedical applications, *Journal of Nanoparticle Research* 13(5), 1917–1927 (2011).
26. M. Boutinguiza et al., Biological hydroxyapatite obtained from fish bones, *Materials Science and Engineering: C*, 32(3), 478–486 (2012).
27. I. Raya et al., Synthesis and characterizations of calcium hydroxyapatite derived from crabs shells (*portunus pelagicus*) and its potency in safeguard against to dental demineralizations, *International Journal of Biomaterials*, 2015, article ID 469176, 1–8 (2015).
28. M. Sivakumar et al., Development of hydroxyapatite derived from Indian coral, *Biomaterials*, 17(17), 1709–1714 (1996).
29. A. F. Lemos et al., Hydroxyapatite nano-powders produced hydrothermally from nacreous material, *Journal of the European Ceramic Society*, 26(16), 3639–3646 (2006).
30. Dariela Núñez et al., Hydroxyapatite nanocrystals synthesized from calcium rich bio-wastes, *Materials Letters*, 230, 64–68 (2018).
31. Y Qi et al., The morphology control of hydroxyapatite microsphere at high pH values by hydrothermal method, *Advanced Powder Technology*, 26(4), 1041–1047 (2015).
32. Xu Xia et al., Synthesis of hollow structural hydroxyapatite with different morphologies using calcium carbonate as hard template, *Advanced Powder Technology*, 29(7), 1562–1570 (2018).
33. Álvaro de Jesús Ruíz-Baltazar et al., Novel biosynthesis of Ag-

- hydroxyapatite: Structural and spectroscopic characterization, *Results in Physics*, 9, 593-597 (2018).
34. D Zhou et al., Comparative study of porous hydroxyapatite/chitosan and whitlockite/chitosan scaffolds for bone regeneration in calvarial defects, *International journal of nanomedicine*, 12, 2673–2673 (2017).
 35. J. Anita Lett et al., Tailoring the morphological features of sol-gel synthesized mesoporous hydroxyapatite using fatty acids as an organic modifier, *RSC Advances*, 9(11), 6228–6240 (2019).
 36. Mohammad Zulhasif Ahmad Khiri et al., The usability of ark clam shell (*Anadara granosa*) as calcium precursor to produce hydroxyapatite nanoparticle via wet chemical precipitate method in various sintering temperature, *SpringerPlus*, 5(1), 1206 (2016).
 37. K. Dhanaraj, G. Suresh, Conversion of waste sea shell (*Anadara granosa*) into valuable nanohydroxyapatite (nHAp) for biomedical applications, *Vacuum*, 152, 222-230 (2018).
 38. Dhiraj Mehta et al., Synthesis of hydroxyapatite nanorods for application in water defluoridation and optimization of process variables: Advantage of ultrasonication with precipitation method over conventional method, *Ultrasonics Sonochemistry*, 37, 56-70 (2017).
 39. Wei Xu et al., The effect of different hydroxyapatite microparticles on the osteogenic differentiation of MC3T3-E1 preosteoblasts, *Journal of Materials Chemistry B*, 6(32), 5234–5242 (2018).
 40. Pujie Shi et al., Characterization of natural hydroxyapatite originated from fish bone and its biocompatibility with osteoblasts, *Materials Science and Engineering: C*, 90, 706–712 (2018).
 41. Nguyen Kim Nga, Nguyen Thi Thuy Chau, Pham Hung Viet, Facile synthesis of hydroxyapatite nanoparticles mimicking biological apatite from eggshells for bone-tissue engineering, *Colloids and Surfaces B: Biointerfaces* 172, 769–778 (2018).
 42. Songkot Utara, Jutharatana Klinkaewnarong, Synthesis and characterization of hydroxyapatite nanoparticles templated by ozonolysed natural rubber latex, *Journal of Sol-Gel Science and Technology*, 80(3), 728–737 (2016).
 43. X Zhao et al., Sintering Behavior and Mechanical Properties of Mullite Fibers/Hydroxyapatite Ceramic, *Materials*, 11(10), 1859–1859 (2018).
 44. Bulat Gabbasov et al., Conventional, pulsed and high-field electron paramagnetic resonance for studying metal impurities in calcium phosphates of biogenic and synthetic origins, *Journal of Magnetism and Magnetic Materials*, 470, 109–117 (2019).
 45. Alexander A. Romanyukha, Marc F. Desrosiers, Dieter F. Regulla, Current issues on EPR dose reconstruction in tooth enamel, *Applied Radiation and Isotopes*, 52(5), 1265–1273 (2000).